Renewable Energy
September 2023, Volume 214, Pages 318-333
https://doi.org/10.1016/j.renene.2023.05.125
https://archimer.ifremer.fr/doc/00840/95211/

Experimental performance and wake study of a ducted twin vertical axis turbine in ebb and flood tide currents at a 1/20th scale

Moreau Martin [1, *], Germain Gregory [1], Maurice Guillaume [2]

[1] Ifremer, Marine Hydrodynamics Laboratory, 150 Quai Gambetta, Boulogne-sur-mer, 62200, France
[2] HydroQuest SAS, 16 Chemin de Malacher, Meylan, 38240, France

* Corresponding author : Martin Moreau, email address : mmoreau@ifremer.fr

ggermain@ifremer.fr ; guillaume.maurice@hydroquest.net

Abstract :

While studies on horizontal axis tidal turbines are plentiful, those on ducted twin vertical axis alike HydroQuest's turbines are lacking. For such a device, both the relative counter-rotation direction of the rotors and the tripod base geometry upstream are different between ebb and flood tide. Consequently, this paper analyses the effect of the two opposed flow directions on the hydrodynamic performance and on the wake of the turbine. The study is based on experimental measurements at a 1/20th scale in Ifremer's wave and current flume tank. The hydrodynamic performance of the model are characterised over a wide range of operating points with the turbine installed on a tripod and on a monopile base. In addition, the 3D wake of the turbine is thoroughly analysed in the two flow directions using 3-component laser Doppler velocimetry. Overall, the drag and the maximum average power coefficient are not affected by the current direction but the optimal tip speed ratio is 7 % lower during ebb with 1.5 times higher power fluctuations compared to flood tide. Besides, the wake of the two rotor columns interact differently depending on the flow direction, leading to a 30 % faster surface averaged velocity recovery in the flood tide configuration. The observed effect of flow direction provides a better knowledge of twin vertical axis turbine wake interactions and highlights the impact of the gravity base geometry on the development of the overall turbine wake. This paper also provides a wide experimental database for the validation of numeric

Highlights

► Ebb and flood tides modelled experimentally in a tank by turning the turbine around. ► Twin vertical axis turbine (2-VATT) mean power is barely affected by flow direction. ► Gravity based 2-VATT power fluctuation and wake development depend on base geometry. ► Rotors wake merging distance and recovery depend on the counter-rotation direction.

Keywords : Tidal energy, Cross-flow turbine, Experimental trials, Laser doppler velocimetry

1. Introduction

After almost two years of testing its 1 MW-rated ducted twin vertical axis tidal turbine (2-VATT) at Paimpol-Bréhat offshore test site, *HydroQuest* wants to validate its design tools to predict the full-scale behaviour of its future turbines (Moreau et al., 2021). To do so, a 1/20th scale model of the demonstrator was designed and tested in the Ifremer wave and current flume tank (Fig. 1). A large database has been generated to compare the turbine behaviour between reduced- and full-scale, and to validate numerical models (Moreau et al., 2022).

Between flood and ebb tides, the current direction is reversed. The relative angle between the two tide directions differs depending on the site considered. It is about 180° in the Alderney race (Furgerot et al., 2020) while it is closer to 160° at Paimpol-Bréhat test site, where the demonstrator was tested. Bottom mounted Horizontal Axis Tidal Turbines (HATT) usually deal with this direction change in two ways (Zhou et al., 2017). The first is to keep the rotor fixed, which implies that it is in the wake of the stanchion in one of the directions, leading to significant performance loss and load fluctuations (Frost et al., 2015). The second is to equip the turbine with a yaw system to maintain the rotor facing the current. This way, the turbine performance remains optimal and constant whatever the flow direction (McNaughton, 2014) but it complicates the system, introducing additional risks of failure (Laws and Epps, 2016). Harrold and Ouro (2019) present rotor loading characteristics of a HATT fixed on a triangular gravity-based foundation with a yaw system. They show a difference in mean rotor loading between ebb and flood tides due to the influence that the asymmetric turbine frame structure and the site bathymetry have on the inflow.

Single isolated Darrieus type VATTs have the advantage to be completely insensitive to the direction of the incident flow. Bachant and Wosnik (2015) and Rolin and Porté-Agel (2018) study the wake of such vertical axis single rotors and find that the average velocity deficit (and so kinetic energy) is asymmetrically distributed in the wake as the deficit is significantly stronger downstream of the rotor side where the blades move against the flow. In addition, the two studies reveal counter-rotating average swirling motions in the planes normal to the flow direction that are the main

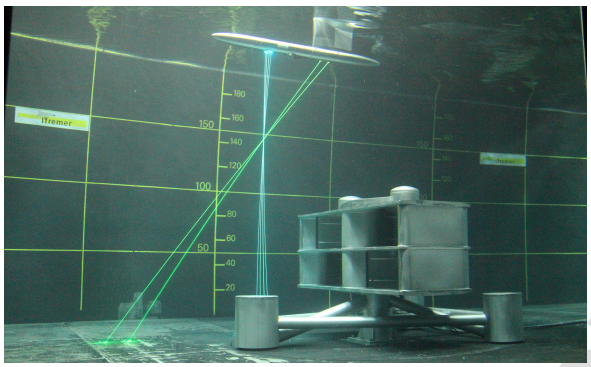

Figure 1: Model of *HydroQuest*'s ducted 2-VATT during 3C-LDV flow measurements in the Ifremer wave and current flume tank.

contributors to the streamwise momentum and average kinetic energy recovery, more importantly than the turbulence. The turbulence kinetic energy distributions are also asymmetrical but in an opposite way between the two studies as Bachant and Wosnik (2015) find the maximal values behind the blades moving downstream whereas Rolin and Porté-Agel (2018) find that maximum behind the blades moving upstream. That difference may be explained by differences of dynamic stall processes due to the rotor geometry differences (foil section, solidity...) and to the different Reynolds numbers.

Several studies reveal that placing two counter-rotating vertical axis turbines side by side improves the power performance significantly (Hill et al., 2014; Vergaerde et al., 2020). In such a twin rotor configuration, however, the device loses the complete insensitivity to the flow direction that characterises isolated VATs. It was shown experimentally on non-ducted twin vertical axis wind turbines that the counter-rotational direction affects the turbine's wake, without affecting significantly the mean power coefficient (Lam and Peng, 2017; Jiang et al., 2020; Müller et al., 2021; Vergaerde et al., 2020). Müller et al. (2021) show that, when the blades move against the flow at the turbine centre, the wakes of the two rotors merge immediately downstream of the turbine and the merged wake expands mainly in the vertical direction; whereas, when the blades move with the flow at the centre, the wakes of the two rotors remain separated and the global wake mostly expands horizontally. Lam and Peng (2017) find similar effects of the relative counter-rotation direction and observe pairs of stationary counter-rotating vortices at both sides of the twin rotors that contribute to the flow mixing. Furthermore, Grondeau et al. (2019) model numerically *HydroQuest*'s ducted 2-VATT tidal turbine wake in 3D without the base during ebb tide and Jégo and Guillou (2021) model it in 2D in both ebb and flood tide flow directions. The relative direction of rotation of the two counter-rotating rotors is reversed between the two current directions as the blades move upstream at the 2-VATT centre during flood tide while they move downstream during ebb tide (Fig. 2). The numerical results show that the power production is insensitive to the flow direction and that the rotor wakes merge faster with a stronger velocity deficit downstream of the central fairing in the flood tide configuration compared to the ebb. However, the numerical models were only validated by comparison to experimental results on a single non-ducted VATT since no results existed for a ducted 2-VATT.

To further validate numerical results and get a deeper insight into the effect of the flow direction on a bottom mounted and ducted 2-VATT, this paper presents an analysis of the experiments on a $1/20^{th}$ scale model of the 1 MW-rated demonstrator in the Ifremer wave and current flume tank. Section 2 first describes the turbine model and its setup in the tank (2.1) before presenting the database acquisition and processing (2.2). Section 3 reports on the flow direction effects on the performance of the 2-VATT in terms of power and drag (3.1) and on the torque angular distribution (3.2). Then, Section 4 presents the effects of the flow direction on the wake of the turbine with regard to its width (4.1), height (4.2), dynamics (4.3) and overall recovery (4.4). Finally, we summarise and discuss the results in Section 5.

2. Material and method

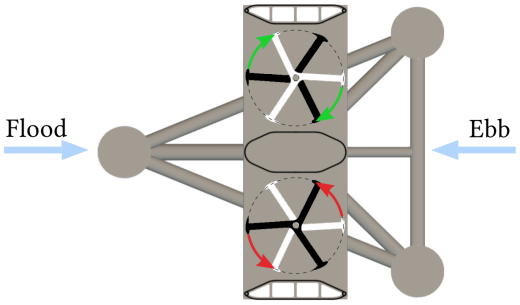

Figure 2: Schematic top view of the ebb and flood tide configurations modelled in the tank with the turbine on the tripod base.

2.1. Experimental setup

The 2-VATT model is geometrically similar to the full-scale demonstrator tested at sea with a scale factor of 1/20 (Moreau et al., 2021). It is composed of two independent counter-rotating vertical axis rotor columns. Each column is made of two levels of Darrieus type rotors with a 60° phase difference between them, and each rotor is made of $N = 3$ blades with NACA 0018 profiles projected on the swept cylinder. The blade height (H_{blade}) is 190 mm. The rotor radius ($R = D/2$) is 200 mm with a blade chord (c) of 73 mm. Thus, the rotor solidity (Nc/R) is 1.1, similarly to the full-scale demonstrator. The columns are mounted in a $W_{struc} = 1.24$ m wide mechanical structure made of fairings and plates. The overall model height, from the floor to the top of the structure is $H_{struc} = 0.84$ m. The turbine height is defined as the distance between the top and the bottom horizontal plates such that $H = 0.45$ m.

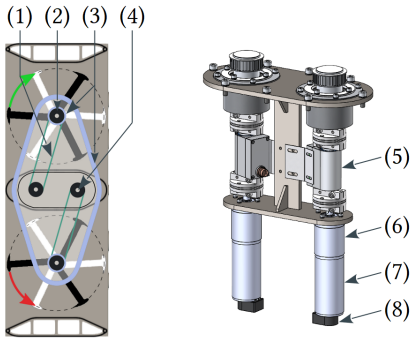

Figure 3: Schematic top view of the twin counter-rotating VATT model on the monopile base, with the transmission system on the top (left). Composition of the secondary shafts, located in the central fairing of the model (right). Caption: (1) Belt; (2) Rotor shaft; (3) Seals; (4) Secondary shaft; (5) Torquemeter with angle encoder *Scaime DR2112-W*; (6) 1/26 reduction gear; (7) DC motor *Maxon RE50*; (8) Rotational speed encoder.

The central fairing of the turbine and the volume inside the top casing are watertight to host the electronics and the transmission system (Fig. 3). Indeed, the rotor shafts are linked to secondary shafts (one for each rotor column) through a belt system on the top of the turbine. Each secondary column is composed of a *Maxon RE50* DC motor equipped with a 1/26th gear reducer and a speed encoder. A *Scaime DR2112-W* torquemeter with a relative angular position encoder is also mounted on the column. The motors are piloted using remote *Escon 70/10* servo-controllers in constant speed mode. In addition, the turbine is fixed on a pseudo-tripod base through a 6-component load cell (*SIXAXES* 1.5 kN, Fig. 4). The tripod structure only models the hydrodynamics of the demonstrator's gravity base. At reduced-scale, the model is actually fixed to the floor of the tank at the bottom of the central pile of the base, right below the turbine, on another 6-component load cell (*SIXAXES* 20 kN) to measure the overall loads on the turbine and the base. The tripod piles are 1 cm above the floor to avoid interferences with the load cell measurements. The reduced-scale turbine can

Experimental study of a ducted 2-VATT in ebb and flood tide currents

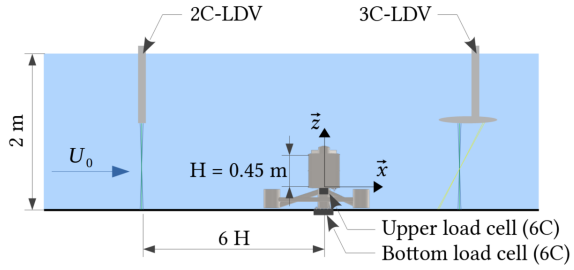

Figure 4: Scheme of the experimental setup in the Ifremer wave and current flume tank (in FC).

Table 1
Recap of the main similitude values between tank tests and in-situ operation at Paimpol-Bréhat.

Scale	H_{wat} (m)	H_{struc} (m)	U (m.s^{-1})	Fr_s	Re_c (at λ = 1.5)
1/20	2	0.84	1.0	0.30	1.0 10^5
1	40	17	2.5	0.17	5.2 10^6

also be fixed on a central monopile of the same height as the tripod and equipped with the same load cells to assess the base influence on the TEC performance and wake.

In this paper, we study the effect of two flow directions representing ideal flood and ebb tides opposed at 180 degrees (Fig. 2). To do so, the turbine and the base are turned around in the tank as the flow direction cannot be reversed. On one hand, in the Flood tide Configuration (FC), the counter-rotating rotor blades move against the flow at the 2-VATT centre, along the central fairing, and the upstream flow encounters a single base pile, aligned with the central fairing of the turbine. On the other hand, in the Ebb tide Configuration (EC), the rotors rotate along with the flow at the centre and the upstream flow encounters two base piles, each aligned with the outer side of the circles swept by the rotors.

The 2-VATT model was tested in the Ifremer wave and current flume tank in Boulogne-sur-mer, France. The water depth is $H_{wat} = 2$ m and the width is $W_{wat} = 4$ m, with a working section of approximately 18 m long (Gaurier et al., 2020). Consequently, the vertical blockage is equal to the one of the demonstrator at the Paimpol-Bréhat test site (41 %) and the projected surface blockage $\left(b = \frac{(HW)_{struc}}{(HW)_{wat}}\right)$ is about 12 % in the tank with the tripod base, and 8 % with the turbine only. According to the literature review by Murray (2016), this surface blockage ratio is at the limit between small enough and too high to consider results as they are. Corrections due to some blockage effects might be needed to estimate performance and wake extent accurately (Bahaj et al., 2007; Ross and Polagye, 2020, 2022).

The orthogonal coordinates system considered is such that x is in the current direction with its origin at the centre of the model and z points towards the surface with its origin at the bottom horizontal plate of the turbine (Fig. 4). The inlet condition in the tank is conditioned by a homogeneous grid and a honeycomb structure. The streamwise average velocity and turbulence intensity profiles at the turbine position in the empty tank are presented in Fig. 5. The streamwise turbulence intensity is defined as $TI_u = \sigma(u)/\overline{u}$, with u the streamwise velocity, the bar on top indicating the time average and $\sigma(\ )$ the time standard deviation of the quantity between brackets. It appears that the boundary layer extends up to the bottom of the turbine, with TI_u decreasing from 7.5 to 1.5 %. The profiles are uniform over the turbine height (between $z/H = 0$ and 1).

The tests were conducted at a current setpoint of 1 m.s^{-1}. At this speed, the Reynolds number based on the blade chord (Re_c) is of the order of 1.0 10^5 in the tank (Eq. 1, with $g = 9.81$ m.s^{-2} the gravity constant, $\nu = 1.05\ 10^6$ m^2.s^{-1} the water kinematic viscosity and λ the tip speed ratio – Eq. 5). At the Paimpol-Bréhat test site, the maximal current speed experienced by the demonstrator was about 2.5 m.s^{-1} which gives a Reynolds number at full-scale about 50 times higher than at reduced-scale (Table 1). The Froude number based on the turbine submergence (Fr_s, Eq. 2) is 1.8 times higher in the tank than at sea but it remains low enough to avoid interactions with the free surface.

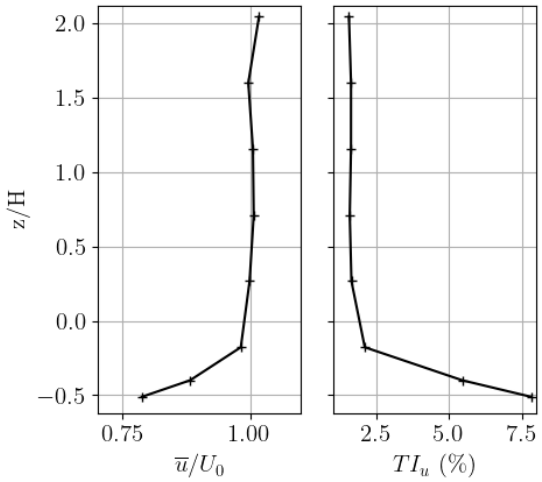

Figure 5: Mean normalised streamwise velocity and turbulence intensity measured with the 3C-LDV probe at $(x, y) = (0,0)$ without turbine.

$$Re_c = \frac{\lambda c U}{\nu} \tag{1}$$

$$Fr_s = \frac{U}{\sqrt{g(H_{wat} - H_{struc})}} \tag{2}$$

2.2. Data acquisition and processing

2.2.1. Performance measurement

For hydrodynamic performance assessment, the current velocity is measured using a *Dantec* 2-Component Laser Doppler Velocimeter (2C-LDV). To do so, the tank is seeded with 10 μm diameter silver coated glass micro-particles. That probe measures the velocity along (x, y) in non-coincident mode (*i.e.* each velocity component is measured independently by each pair of lasers) with an acquisition data rate of the order of 200 Hz. The probe is placed at $x/H = -6$ and at the centre of the turbine projected area (ie. $(y, z) = (0, 0.5)H$). The mean streamwise component of the velocity at this point is considered as the reference velocity (noted U_0) and is 0.95±0.02 m.s^{-1} overall. Fig. 6 shows that the upstream flow is undisturbed by the TEC induction from this position. In addition, it also shows that the incident flow tends to avoid the turbine with a vertical velocity component value up to $0.05U_0$ at $x/H = -2$. As expected, the lateral component of the incident velocity is null at this point (centre of the tank and of the projected area of the turbine).

Synchronously with the 2C-LDV, each rotor column torque (Q), rotational speed (ω) and the two load cell signals are acquired using *National Instruments PXI* and *LabView* systems. The acquisitions last 3 minutes with a 128 Hz sampling frequency for each run to guarantee the time convergence of the mean and standard deviation of the signals. The performance results are presented in terms of power coefficient (C_P) and drag coefficient (C_x) with regard to the tip speed ratio (λ), defined in Eq. 3 to 5; with $\rho = 1000$ kg.m^{-3} the density, P the power extracted by the two columns $\left(P = \sum \omega Q\right)$ and F_x the load in the streamwise direction measured by the upper load cell (Fig. 4). The reference surface considered is the projected area of the four rotors $\left(4DH_{blade}\right)$.

$$C_P = \frac{P}{2\rho D H_{blade} U_0^3} \tag{3}$$

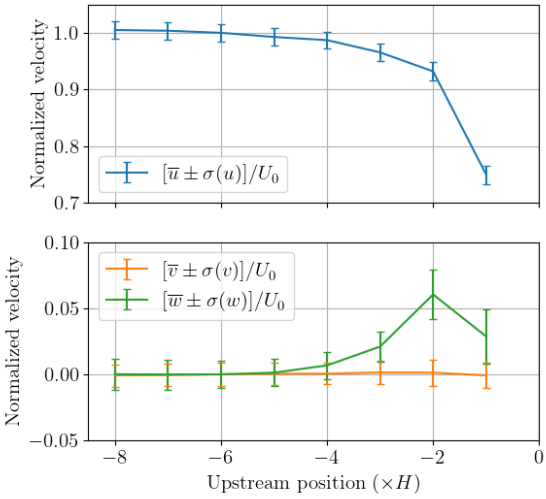

Figure 6: Flow velocity measured upstream of the model in flood tide configuration at the centre of the turbine ($(y, z) = (0, 0.5H)$) and varying x positions using the 3C-LDV. Normalized streamwise velocity u at the top and transverse velocities (v, w) at the bottom.

$$C_x = \frac{F_x}{2\rho D H_{blade} U_0^2} \tag{4}$$

$$\lambda = \frac{\omega R}{U_0} \tag{5}$$

The distribution of the torque coefficient (C_Q, Eq. 6) with regard to the rotor angular position of the green column (Fig. 2) is also analysed. The instantaneous relative angular position (positive in the rotational direction) is computed by Hilbert transform of the torque filtered at the rotational frequency ± 0.005 Hz. The angular position being relative, the absolute angle values displayed cannot be compared between graphs. The phase-average torque coefficient, $\widetilde{C_Q}$, is computed over 75 revolutions with 3° angle bins. The reference surface for the computation of C_Q is the projected area of a single rotor column ($2DH_{blade}$).

$$C_Q = \frac{Q}{\rho D H_{blade} R U_0^2} \tag{6}$$

2.2.2. Wake measurement

The flow surrounding the ducted 2-VATT is characterised in the two flow directions at the same operating point ($\lambda = 1.6$) using *Dantec* 3-Component LDV, in non-coincident mode. Upstream of the turbine, the flow is mapped following the mesh of measurement points presented in Fig. 7 (a) at $x/H = \{-1, -2\}$. At $x/H = -1$, the geometry of the 3C-LDV makes it unable to measure the points from $z/H = 0.0$ to 0.5. Therefore, only (u, v) are measured by the 2C-LDV at those positions. Downstream, we assumed the wake to be symmetrical so we mapped the flow following the mesh in Fig. 7 (b) at $x/H = \{2, 3, 5, 7, 9\}$. At $x/H = 1$, the same mesh is mapped without the bottom line as the 3C-LDV probe would collide with the model. At $x/H = 0$, the top lines at $z/H = \{1.6, 2.0\}$ and the side ones at $y/H = \{2.1, 2.8\}$ are measured.

Given the LDV operating principle (Boutier, 2012), the velocity is measured every time a seeding particle passes through the measurement volume. Therefore, the acquisition rate ranges between about 50 and 300 Hz, where the mean velocity is low and high respectively, depending on the position in the 2-VATT wake. Given the orientation of

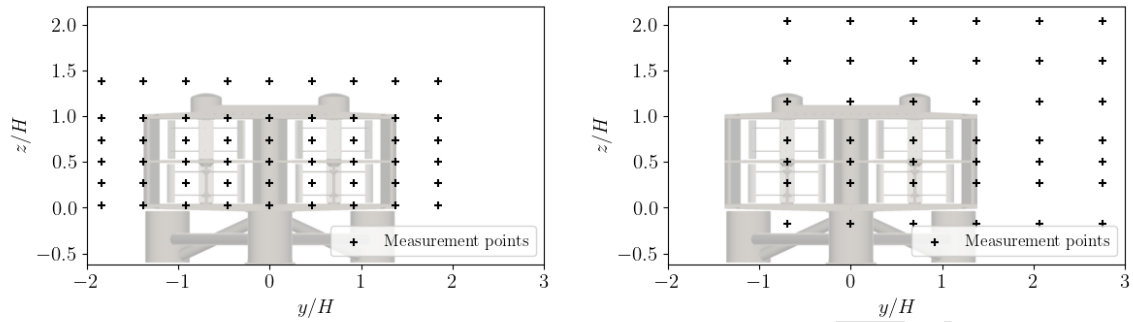

(a) Upstream mesh (b) Downstream mesh

Figure 7: Meshes used for velocity measurements by the 3C-LDV at a given x positions.

the three pairs of lasers composing the 3C-LDV (Fig. 1), it is necessary to project the lasers measurements into the tank coordinate system to get the velocities (u, v, w) along (x, y, z). To do so, the measurements in the lasers coordinates system are interpolated on the same time vector (that matches the lowest data rate of the 3 pairs of lasers) to apply the transformation matrix.

The velocity contours presented hereinafter are drawn based on linear interpolations between the mesh points with a 40 mm step in the y and z directions, and 50 mm in the x direction. Ebdon et al. (2021) suggest that several complementary metrics are needed to characterise a tidal turbine wake as it is difficult to develop quantitative metrics by which to quantify simultaneously the strength of the wake as well as the region it affects. To look at the region affected by the 2-VATT, the wake width and height are computed at each x position measured, using the interpolated velocity flow fields in the (y, z) planes. As is commonly done in the literature (Masters et al., 2013; Ahmadi, 2019; Ebdon et al., 2021), a velocity threshold at $\overline{u}/U_0 = 0.9$ is defined to locate the wake boundary and analyse its shape. The half wake width is computed as the horizontal position where $\overline{u}/U_0 = 0.9$ averaged over the turbine height ($0.00 < z/H < 1.00$) and the wake height is computed as the vertical position of the velocity threshold averaged over the half turbine width ($0.00 < y/H < 1.38$). To look at the wake strength and its recovery at each x position measured, we compute surface averages of the time averaged streamwise velocities, noted $< \overline{u} >$, downstream of the turbine. Two surfaces in the (y, z) planes are considered to provide complementary information. The first one is the projection of the half capture area of the turbine $\left(< \overline{u} >_{cap}\right)$. The projection of the capture area is commonly used in the literature to assess the wake recovery and study turbine's interactions in an array (Mycek et al., 2014; Ebdon et al., 2021). That area is constant at all the x positions so it ignores all the wake expansion outside that restricted area. The second averaging area is the one where $\overline{u}/U_0 < 0.9$ $\left(< \overline{u} >_{0.9}\right)$. That area changes with x but it quantifies the strength of the velocity deficit in the whole region affected by the turbine wake, in contrast to $< \overline{u} >_{cap}$. Finally, contours of turbulent kinetic energy, defined in Eq. 7, are also analysed at the different x positions measured, with the same interpolation steps as for the velocity contours.

$$k_{UV} = \frac{1}{2}(\sigma(u)^2 + \sigma(v)^2) \tag{7}$$

3. Flow direction effect on the hydrodynamic behaviour of the ducted 2-VATT

To characterise the hydrodynamic behaviour of the ducted twin vertical axis tidal turbine in the tank and the effect of the flow direction, whether similar to Flood tide Configuration (FC) or to Ebb tide Configuration (EC), the overall turbine performance is studied before addressing the angular distribution of the torque generation.

3.1. Overall performance

The mean and standard deviation of the drag coefficient and the normalised power coefficient (Eq. 3 & 4) are presented in Fig. 8 with regard to the tip speed ratio (Eq. 5). Each curve is the average over 3 test campaigns and the

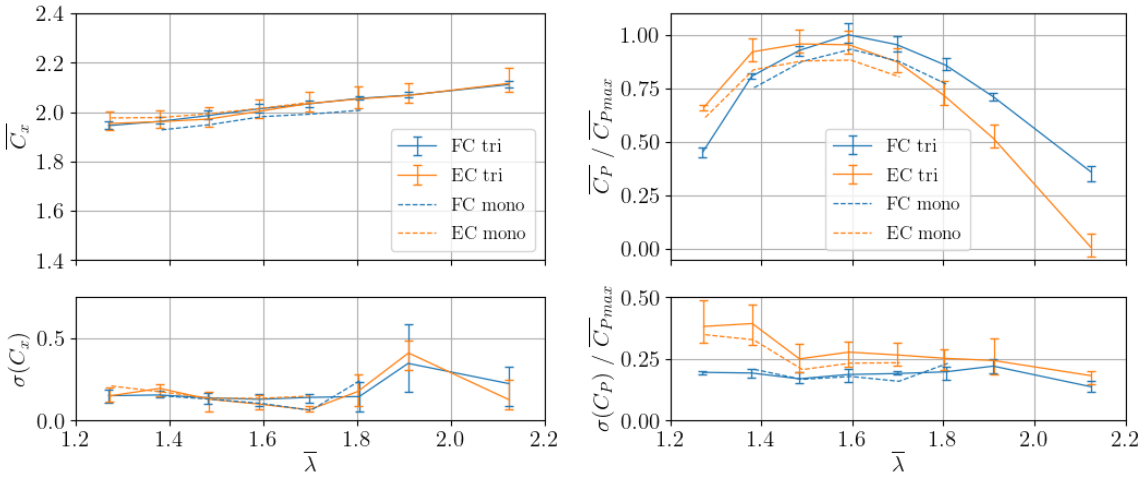

Figure 8: Average (top) and standard deviation (bottom) of th drag (a) and power (b) coefficients in FC and EC on the tripod base and on the monopile base. Each curve is an average over 3 test campaigns with the error bars representing the extreme average and extreme standard deviation values over the 3 campaigns.

error bars represent the extreme average or extreme standard deviation values among these campaigns. The amplitude between extreme average values is less than 5 % for $\overline{C_x}$ and about 10 % for $\overline{C_P}$ at the maximal performance point. Fig. 8(a) reveals that the drag coefficient of the 2-VATT is similar in flood and ebb tide configurations, both in terms of average and fluctuation, no matter the base geometry. We notice that 60 % of the average drag coefficient is composed of the rotors thrust and the other 40 % is due to the friction drag on the structure as the $\overline{C_x}$ measured without rotors is about 0.8. The maximal $\overline{C_P}$ value is also hardly affected by the flow orientation (4 % difference in average over the 3 campaigns). However, the optimal λ is clearly lower and the power standard deviation is 1.5 times higher in average over the λ range in ebb tide than in flood tide configuration. The results with the turbine fixed on the central monopile show the same shift in the optimal λ between the two flow directions. Therefore, this result is due to the difference of relative counter-rotation direction rather than to the tripod base asymmetry. The average power extracted with the turbine on the monopile appears lower than with the turbine on the tripod; this is probably due to the lower projected area of the whole model which induces a lower blockage ratio and so a lower flow through the turbine. Besides, the gap of power fluctuations between EC and FC narrows when the turbine is fixed on the monopile. The effect of the flow orientation on the power production can be further explained by looking at the torque angular distribution on one column of rotors.

3.2. Torque angular distribution

Fig. 9 displays the normalised torque coefficient with regard to a relative angular position at the optimal λ (at which $\overline{C_P}$ is maximal) in the two configurations, on the tripod base (a & b) and on the monopile (c & d). The overall averaged C_Q is equal between EC and FC. For all the cases, we observe six torque peaks corresponding to the contribution of each blade as one rotor column is made of two levels of 3 bladed rotors with 60 degrees shift between them. However, with the tripod base, the rose shape differs significantly between the two configurations. The torque distribution in EC shows clearer peaks and reveals an asymmetry between the top and the bottom rotors whereas the torque distribution is much smoother in FC. Consequently, the standard deviation of $\widetilde{C_Q}$ is 1.8 times higher in EC than in FC, which directly leads to the $\sigma(C_P)$ gap observed in Fig. 8(b). Fig. 9 (c & d), with the monopile, show that the torque distribution in FC is unchanged compared to the case with the tripod but that the asymmetry between the top and the bottom rotors in EC disappears. Consequently, the standard deviation gap between the two configurations narrows. It still remains a 1.25 ratio between $\sigma(\widetilde{C_Q})$ in EC compared to FC as the contribution of each blade remains more marked.

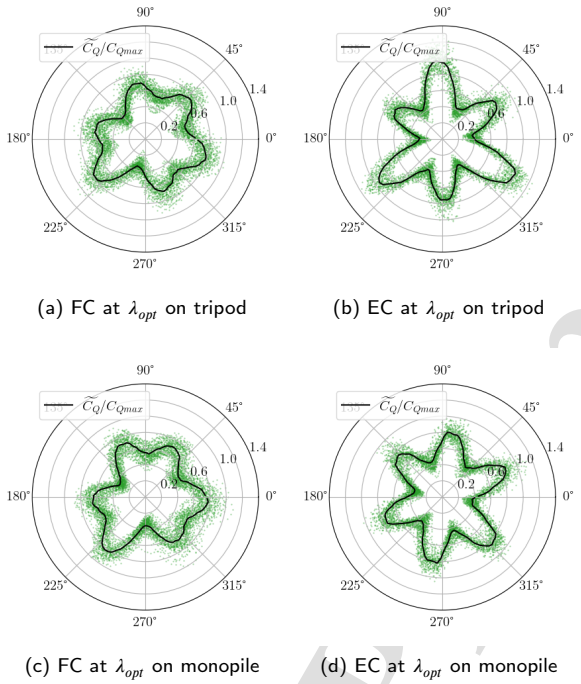

(a) FC at λ_{opt} on tripod (b) EC at λ_{opt} on tripod

(c) FC at λ_{opt} on monopile (d) EC at λ_{opt} on monopile

Figure 9: Angular distribution of the torque coefficient for the green rotor column at the optimal λ for the two flow orientations (1.6 in FC, 1.5 in EC). Torques are normalised by the maximal phase-average value, measured in EC on the tripod base. The green dots are the instantaneous measurements and the black line is the phase average. *Reminder*: the angular position is relative, so the absolute angle values cannot be compared between graphs.

In EC, the base feet are aligned with the outer part of the rotors (Fig. 2 and 7). The streamwise velocity profiles in Fig. 10 show that the flow deflection around the tripod structure upstream generates an overspeed in front of the bottom rotors compared to the case on the monopile. That overspeed exceeds the average velocity in front of the upper rotor so we assume the highest $\widetilde{C_Q}$ peaks to be generated by the bottom rotor. Besides, the velocity standard deviations are between 3 and 5 times stronger above the two base feet compared to the case on the monopile at the same positions. Those two observations can explain the difference of torque angular distribution, and therefore of power coefficient fluctuations, in EC between the case on the tripod and on the monopile. Conversely, in FC, the central base foot upstream is aligned with the central fairing of the turbine. The flow deflection around that foot does not impact much the rotors which explains the absence of difference torque angular distribution and power coefficient fluctuations between the cases on the tripod and on the monopile base.

4. Flow direction effect on the wake of the ducted 2-VATT

Beyond the effects on the hydrodynamic behaviour of the turbine, this section aims at analysing how opposed flow directions between ebb and flood tide can affect the wake of the ducted 2-VATT. The latter is studied in terms of width, height, dynamics and recovery. All the velocity contours and profiles presented in this section with the turbine on the tripod base are also displayed in FC on the monopile base in Appendix A to contribute to the discussion of the results and provide an extended database for numerical model validation.

4.1. Wake width evolution

Fig. 11 displays average streamwise velocity contours of the wake at different altitudes downstream of the turbine in FC and EC on the tripod base. It reveals significant wake differences between the two configurations at the first glance. In the near wake, down to $x/H = 3$, the maximal velocity deficits are located behind each rotor column over

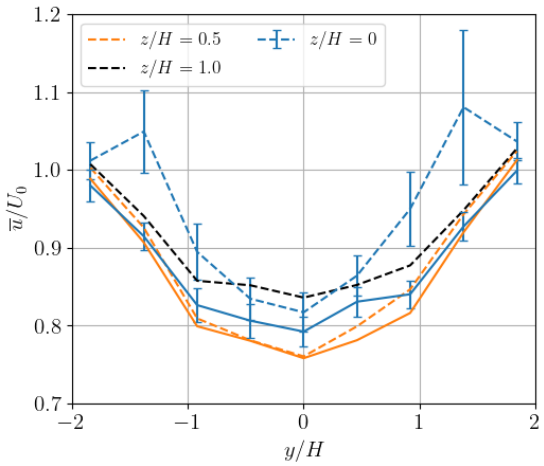

Figure 10: Streamwise velocity profiles measured by LDV upstream of the turbine at $x/H = -1$ in EC, with the turbine on the tripod base (dashed lines) and on the monopile (solid lines). This x position is located above the tripod feet in EC (Fig. 11). The error bars represent the normalized standard deviation of the streamwise velocity.

the turbine height in the two configurations. However, the velocity deficits behind each column merge at $x/H = 3$ in FC (i.e. a single maximal deficit at $y/H = 0$) while they merge past $x/H = 5$ in EC at $z/H = 0.50$ (Fig. 12). This is due to the difference of counter-rotation since the merging distance in FC on the monopile base is similar to that on the tripod (Appendix A).

Besides, Fig. 11 (i & j) show that the wake boundary ($\overline{u}/U_0 = 0.9$) of the tripod base expands laterally in FC up to $y/H = 2.0$ while it remains of constant width in EC from $x/H = 3$ to 9 at $y/H = 1.8$. Overall, Fig. 13 presents the half wake width averaged over the turbine height ($0.00 < z/H < 1.00$) with regard to the downstream position in EC and in FC on the tripod and the monopile base. It reveals that the base wake strongly interferes with the turbine wake, leading to an increase of the turbine wake width in FC on the tripod from $x/H = 2$ to 7 while it only decreases on the monopile and in EC. In the end, at $x/H = 9$, the wake is 5 % wider in FC on the tripod base than in EC on the tripod and is 31 % wider in FC on the tripod than in FC on the monopile base. Thus, despite the clear difference of wake merging distance due to the opposed counter-rotation direction, the turbine wake width appears to be more affected by the base geometry than the rotation direction. Furthermore, Fig. 11 (a & b) show that the wake expands more vertically in EC than in FC. The next section deals with this topic in depth.

4.2. Wake height development

Fig. 14 displays average streamwise velocity contours of the wake at different lateral positions in FC and EC on the tripod base. Firstly, Fig. 14 (a & b) highlight the effect of the base asymmetry in the plane of the turbine edge ($y/H = 1.38$), showing from another point of view the larger spreading of the wake in FC, as discussed in the previous section. These contours also show that the turbine wake is more intense in this plane down to $x/H = 3$ in EC. In addition, by subtracting the velocity field measured in the wake of the turbine on the monopile to the one measured downstream of the turbine on the tripod in the same operating conditions, we can observe that the wake of the base influences that of the turbine over the whole turbine height (Fig. 15). In the far wake, the tripod base is responsible for about 20 % more velocity deficit at the height of the bottom rotors compared to the case on the monopile.

Secondly, the velocity fields in the plane of the central fairing of the turbine ($y/H = 0.00$) strongly differ between EC and FC (Fig. 14 (e & f)). The velocity profiles in this plane, plotted in Fig. 16, show with more precision that the average velocity profiles are of similar shape right behind the turbine, at $x/H = 1$. However, from $x/H = 2$ to 5, the velocity profiles in EC present a maximum at half the turbine height that is absent in FC. This downstream distance interval corresponds to the positions where the wakes of the two rotor columns have already merged in FC whereas they are still separated in EC, as shown in the previous section. Once the wakes are merged in the two configurations, past $x/H = 5$, the velocity profiles present similar shapes but the velocity gradient is steeper in FC. The velocity is

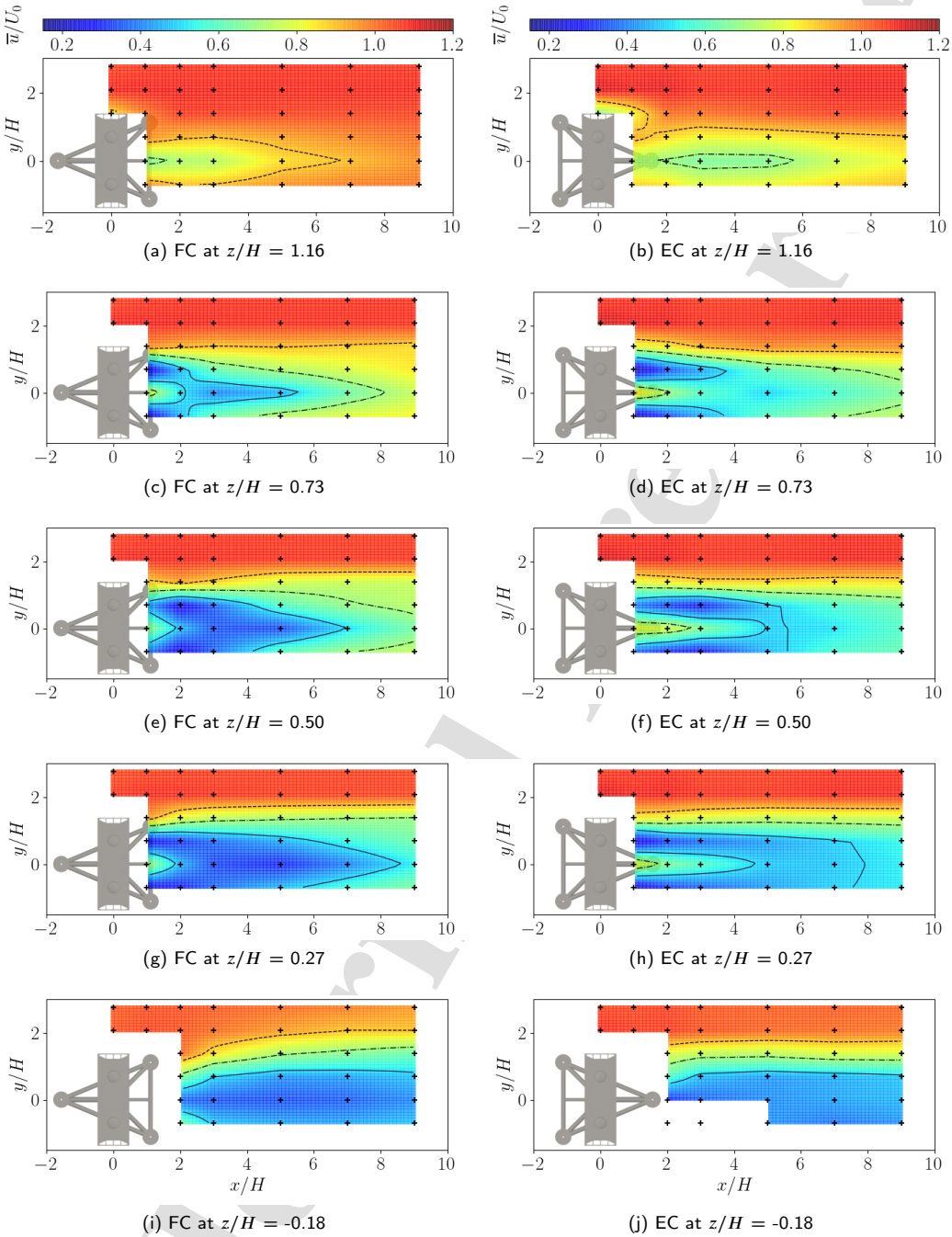

Figure 11: Contours of the normalised average streamwise velocity $\left(\overline{u}/U_0\right)$ in (x, y) planes at different vertical positions, in FC on the left and in EC on the right. The black crosses show the measurement point positions; the dashed, dash-dot and solid lines are iso-contours of $\overline{u}/U_0$ = 0.9, 0.7 and 0.5 respectively. The lacking points in (j) are due to some air bubble releases from model cavities that resulted in poor quality measurements.

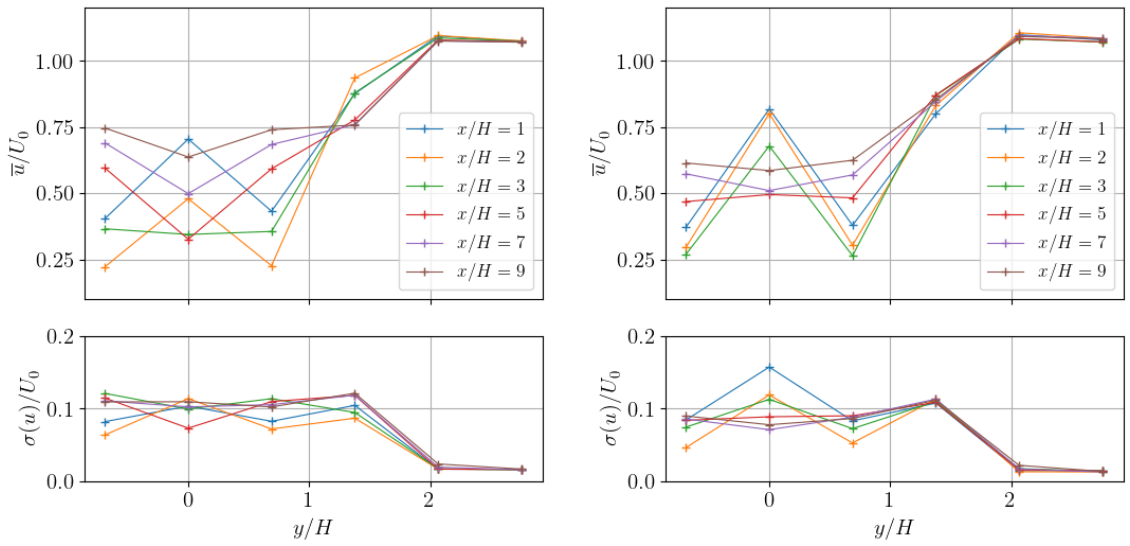

(a) Flood tide Configuration

(b) Ebb tide Configuration

Figure 12: Horizontal streamwise velocity profiles at the centre of the turbine ($z/H = 0.5$) and at different downstream distances, in FC on the left and in EC on the right.

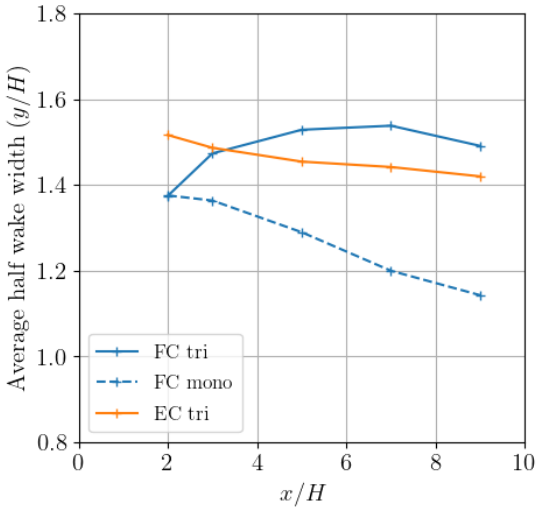

Figure 13: Average half wake width ($\overline{u}/U_0 = 0.9$) over the turbine height ($0.00 < z/H < 1.00$) as a function of the downstream distance in FC and EC on the tripod base, and in FC on the monopile base.

about 1.2 times higher at $x/H = 9$ in FC than in EC at the top of the turbine ($z/H = 1$) while it is equal at the turbine bottom. Consequently, the vertical shear layer between the wake maximal velocity deficit and the faster free-stream velocity is much thinner in FC than in EC. Besides, the overall maximal velocity deficit over the turbine height in that centre plane is located at $x/H = 5$ and $z/H = 0.27$ in both configurations, but it is 56 % higher in FC $\left(\overline{u}/U_0 = 0.27\right)$ than in EC $\left(\overline{u}/U_0 = 0.48\right)$.

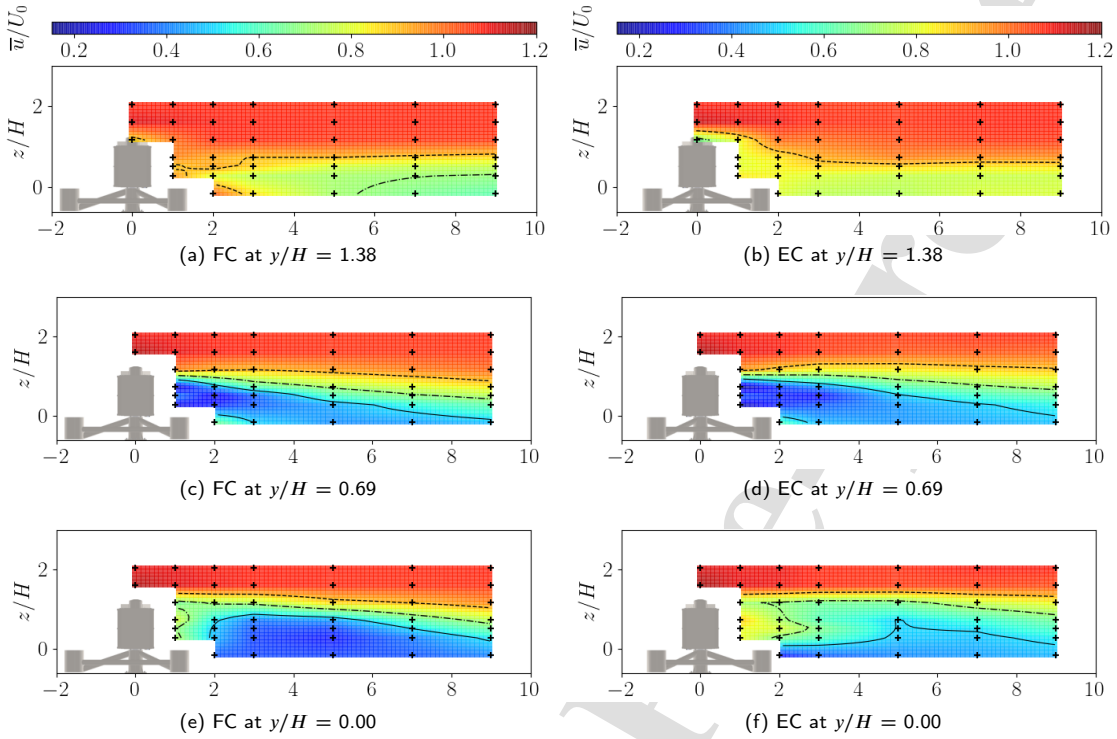

Figure 14: Contours of the streamwise velocity $(\overline{u}/U_0)$ in the (y, z) plane at different positions along the width, in FC on the left and in EC on the right. The black crosses show the measurement point positions; the dashed, dash-dot and solid lines are iso-contours of $\overline{u}/U_0 = 0.9$, 0.7 and 0.5 respectively.

Thirdly, the streamwise velocity deficit behind the rotors($y/H = 0.69$) appears quite similar in EC and FC (Fig. 14 (c & d)). Despite this relative similarity, the wake height of the three iso-velocity contours displayed ($\overline{u}/U_0 = 0.9$, 0.7 and 0.5) are lower in FC than in EC, which also reveals a thinner vertical shear layer in FC. This trend of wake height remains true when looking at the average over the half turbine width ($0.00 < y/H < 1.38$, Fig. 17). Indeed, the wake is from 8 % higher at $x/H = 1$ to 20 % higher at $x/H = 9$ in EC than in FC overall, which also indicates that the wake height decreases faster in FC. The comparison to the results on the monopile shows no difference in the near wake and only a slight influence of the base on the vertical expansion in the far wake as it keeps decreasing faster on the monopile. Consequently, unlike the width, the wake height appears to be more influenced by the difference of relative counter-rotation direction than by the base geometry.

4.3. Wake dynamics

Fig. 18 presents superimpositions of mean streamwise velocity contours and arrow fields of the mean transverse velocities $(\overline{v}, \overline{w})/U_0$ in (y, z) planes at different downstream positions, in FC and EC. Beyond the observations on the wake width and height made previously, the arrow fields reveal two large swirls around the x axis behind each rotor column in the two flow configurations. Those swirls are more structured in FC and persist much further downstream in the wake as they are still clearly visible at $x/H = 9$, unlike in EC. Indeed, the maximal transverse velocities in FC are of the order of 2 times those in EC at $z/H = 0.73$ behind the rotors (Fig. 19).

Fig. 20 & 21 display contours of the normalized 2D turbulent kinetic energy (k_{UV}, Eq. 7) in (y, z) planes at the 6 downstream positions. Both in FC and EC at $x/H = 1$, similarly to the results of Bachant and Wosnik (2015) in the near wake of a single high solidity VATT, the turbulent kinetic energy is low at the rotors centre. The high levels of k_{UV} are focused around the y boundaries of the rotors, where the blades undergo dynamic stall. However, the mesh of LDV measurement points used in this work (Fig. 7) is too coarse to locate precisely the k_{UV} maxima and separate

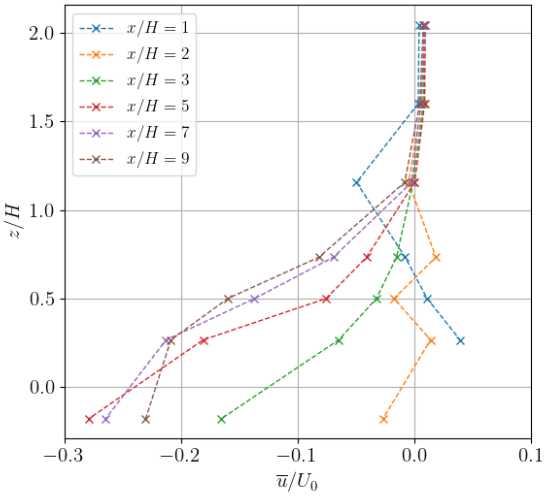

Figure 15: Difference of streamwise velocity at $y/H = 1.38$ between the wake downstream of the turbine in FC on the tripod and on the monopile base, along vertical profiles at different downstream distances.

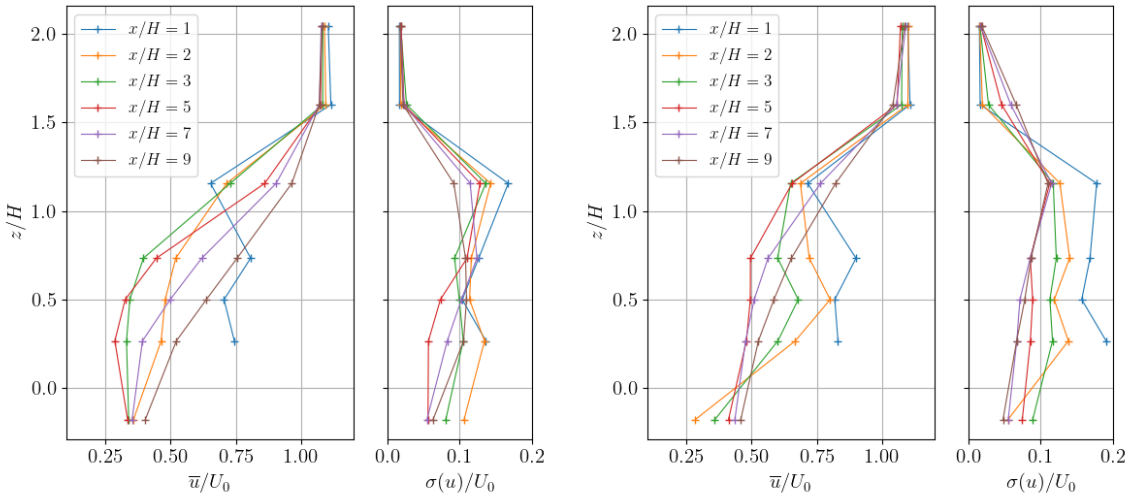

(a) Flood tide Configuration

(b) Ebb tide Configuration

Figure 16: Vertical streamwise velocity profiles at the centre of the turbine ($y/H = 0.00$) and at different downstream distances at the centre of the turbine, in FC on the left and in EC on the right.

the contribution of the blades from that of the support structure, the minimal gap between the blades and the vertical plates being less than 2 cm. Furthermore, we observe that k_{UV} is more intense in the near wake ($0 < x/H < 3$) in EC than in FC, especially at the height of the turbine top lid. The 3C-LDV measurements upstream of the turbine, at $x/H = -1$, reveal a stronger vertical flow bypassing in EC than in FC. The vertical velocity component at $(y, z)/H = (0,1)$ is almost $0.2U_0$ in EC, which is 15 % higher than in FC. As a result, the top horizontal plate of the turbine faces a current with a greater angle of incidence in EC that may cause larger flow detachment in the wake of the top lid and explain the higher levels of turbulent kinetic energy at this location. At $x/H = 3$, k_{UV} peaks are smoothed and the turbulent kinetic energy is more spread on the whole turbine projected area in the two flow configurations. Then, in

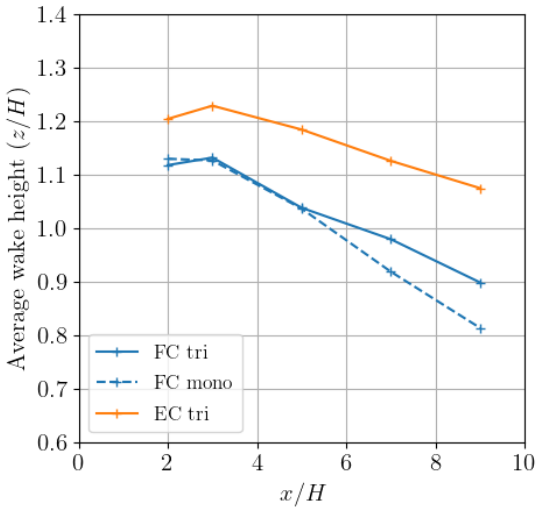

Figure 17: Average wake height of $\overline{u}/U_0 = 0.9$ over the half turbine width ($0.00 < y/H < 1.38$) as a function of the downstream distance in FC and EC on tripod, and in FC on monopile.

the far wake, k_{UV} is gradually dissipated and it remains mostly in the average velocity shear layer. Since that shear layer is thinner in FC than in EC (Fig. 18), the turbulent kinetic energy is focused in a thinner area in FC and so the maximum k_{UV} is higher in FC than in EC in the far wake.

4.4. Wake recovery

To sum up, Fig. 22 (a) presents the evolution of the velocity averaged over the area where $\overline{u}/U_0 < 0.9$, noted $< \overline{u} >_{0.9}$, with the downstream distance in EC and FC (on the tripod and the monopile base). This quantity reveals the strength of the velocity deficit over the whole wake region. The comparison of the two curves in FC shows that the base geometry is responsible for the initial velocity deficit, right behind the 2-VATT, which is stronger with the turbine on the tripod base than on the monopile. Then, the base does not influence the recovering dynamics of the wake, so the initial velocity difference remains in the far wake. Besides, the strength of the wake appears significantly lower in EC than in FC in the near wake. As the recovery rate appears smaller in EC than in FC, the relative strength of the deficit reverses in the far wake between the two flow configurations and the average deficit ends up stronger in EC than in FC.

Finally, Fig. 22 (b) presents the evolution of the velocity averaged over the projected half turbine capture area $\left(< \overline{u} >_{cap}\right)$ with the downstream distance in EC and FC (on the tripod and the monopile base). First, the velocity decreases between $x/H = 2$ and 3 with the tripod base in the two flow configurations and not with the monopile. This shows the contribution of the tripod base to the turbine wake. Then, past $x/H = 3$, the velocity recovers following a linear trend with the downstream position in the three cases. By extrapolation of these linear trends, $< \overline{u} >_{cap}$ would recover $\overline{u}/U_0 = 0.9$ at $x/H \simeq 20$ in the ebb tide configuration with the tripod base, at $x/H \simeq 16$ in the flood tide configuration with tripod base and at $x/H \simeq 12$ with the monopile base in FC. Thus, it appears that the FC recovers about 30 % faster than the EC. That result can be explained by the stronger average transverse velocities $(\overline{v}, \overline{w})$ in FC revealed previously (Fig. 18). Indeed, the measurements of Bachant and Wosnik (2015) and Rolin and Porté-Agel (2018) in the wake of single vertical axis turbines also reveal pairs of counter-rotating average swirling motions propelling fluid downward towards the turbine centerline. Their analyses of the mean and turbulent kinetic energy budgets show that these swirls are the main contributors to the streamwise momentum and average kinetic energy recovery, more importantly than the turbulence.

Besides, the velocity recovery behind the ducted 2-VATT is about 20 % faster with the monopile base than with the tripod mainly thanks to the higher flow velocity between the tank floor and the turbine wake that can contribute to filling the velocity deficit faster (Appendix A, Fig. 25).

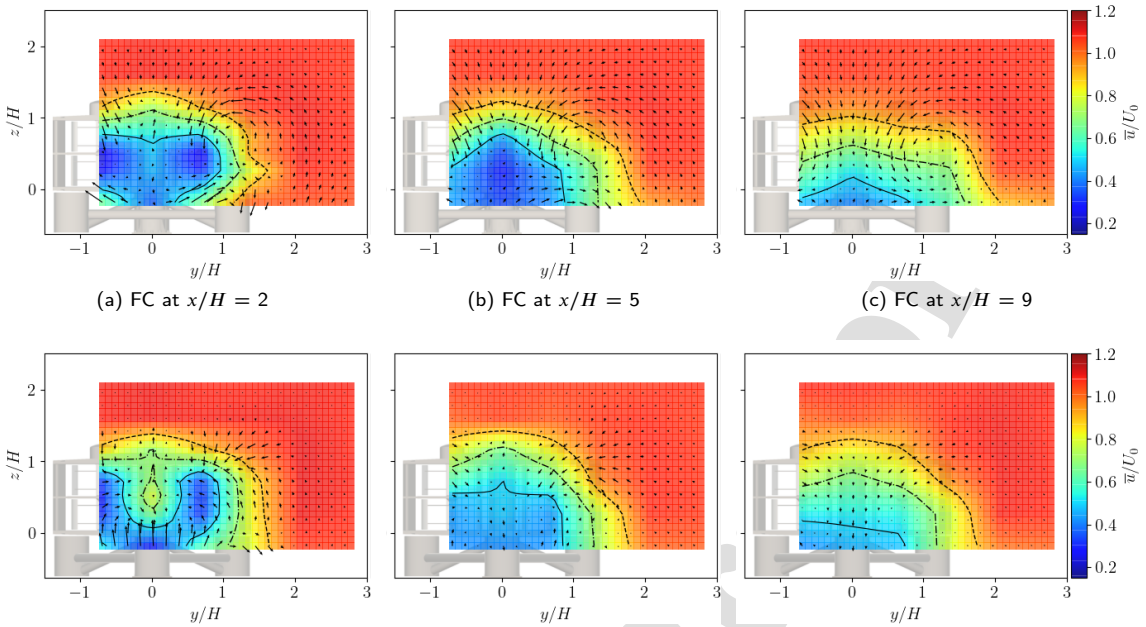

(a) FC at $x/H = 2$ (b) FC at $x/H = 5$ (c) FC at $x/H = 9$

(d) EC at $x/H = 2$ (e) EC at $x/H = 5$ (f) EC at $x/H = 9$

Figure 18: Contours of the mean streamwise velocity $(\overline{u}/U_0)$ in (y, z) planes at 3 downstream positions, viewed from downstream, with superimposition of arrow field of the mean transverse velocities $(\overline{v}, \overline{w})/U_0$; the dashed, dash-dot and solid lines are iso-contours of $\overline{u}/U_0 = 0.9$, 0.7 and 0.5 respectively.

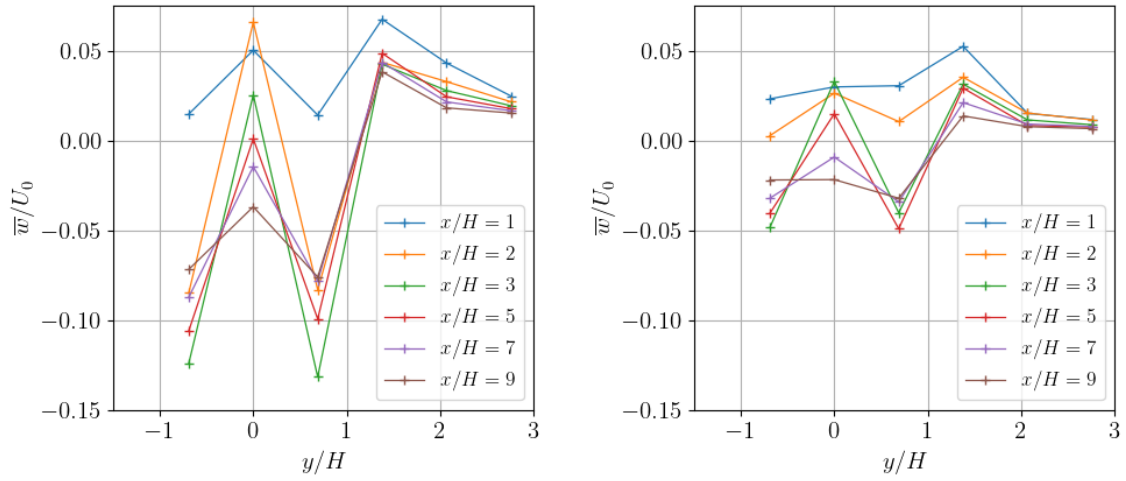

(a) Flood tide Configuration (b) Ebb tide Configuration

Figure 19: Horizontal profiles of mean vertical velocity at different downstream distances and $z/H = 0.73$, in FC on the left and in EC on the right.

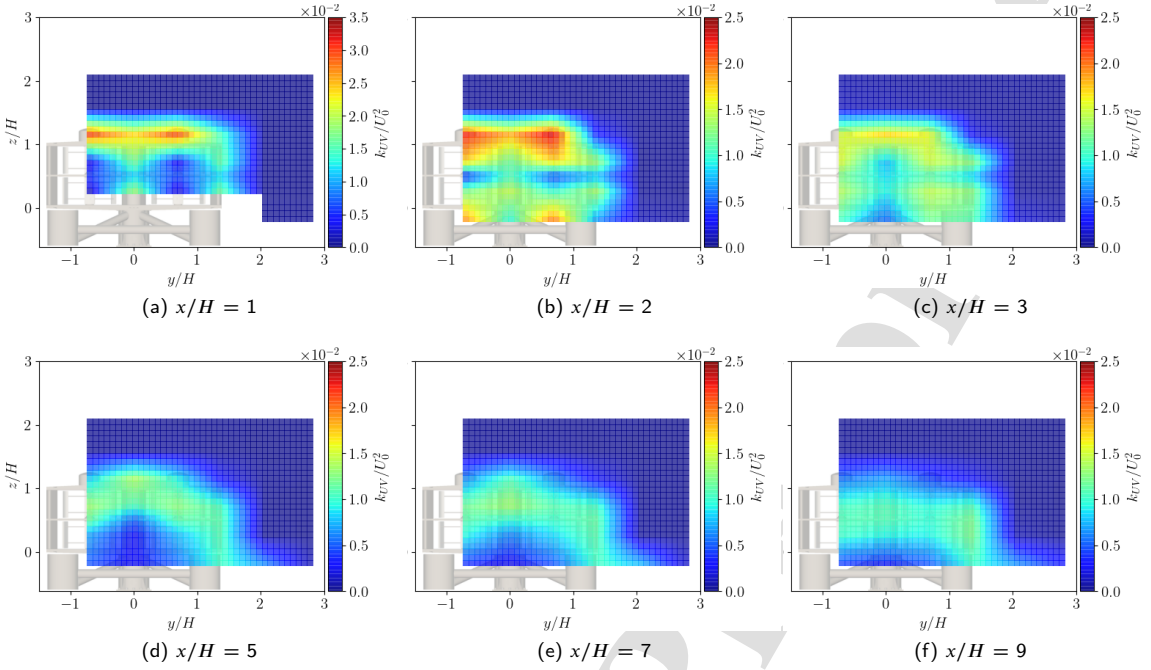

Figure 20: Flood tide Configuration - Contours of the turbulent kinetic energy computed on u and v viewed from downstream. *nb*: the color scale is different in (a) compared to others.

5. Discussion and conclusions

The results presented in Section 3 show that the drag of the turbine is not significantly affected by the flow direction nor the maximal average power coefficient. However, the optimal tip speed ratio is 7 % lower in EC ($\lambda_{opt} = 1.5$) compared to FC ($\lambda_{opt} = 1.6$), due to the difference of relative counter-rotation direction of the two rotor columns; and the power fluctuations are about 1.5 higher in EC, explained by stronger torque variations along a revolution. Jégo and Guillou (2021) simulated numerically the same turbine at full-scale with a model based on a 2D actuator cylinder method. They calculated the power output in the two flow directions with the turbine operating at $\lambda = 2$ and found no difference between the two cases. This is not consistent with the present work as we find a ratio of 1.9 between the average power coefficient in FC and in EC at this λ. Given the method used, the numerical model does not take into account the losses due to blade tips, the rotor arms and the shafts. The absence of these dissipation phenomena leads to an overestimation of the optimal tip speed ratio (Guillaud, 2017). Then, assuming that $\lambda = 2$ is the optimal operating point with the numerical model (not specified by Jégo and Guillou (2021)), the absence of flow direction effect on the maximal average power coefficient would be coherent with our experimental results.

Secondly, regarding the flow downstream of the turbine presented in Section 4, the far wake in EC appears to be slightly less wide (5 %) than in FC, mainly due to the tripod base asymmetry, but higher (10 to 20 %), mostly caused by the difference of relative counter-rotation direction. The trends of horizontal and vertical expansion are the opposite to what is presented on the non ducted twin vertical axis wind turbine by Müller et al. (2021), which highlights the effect of the fairings and the base geometry on the turbine wake development. Besides, the flow direction strongly affects the interaction between the wakes of the two rotor columns as they merge further in EC than in FC ($x/H = 5$ and 3 respectively). Given the counter-rotation direction in EC and FC, the difference of merging distance tendency is consistent with the results obtained in the wake of a non-ducted twin vertical axis wind turbines in a tunnel (Lam and Peng, 2017; Vergaerde et al., 2020; Müller et al., 2021) and with the 2D numerical simulations of the same ducted 2-VATT (Jégo and Guillou, 2021).

Thirdly, the 3C-LDV mapping of the flow reveals large swirling motions around the x axis behind each rotor column in the two configurations. Grondeau et al. (2019) modelled the wake of the ducted 2-VATT without base nor generator

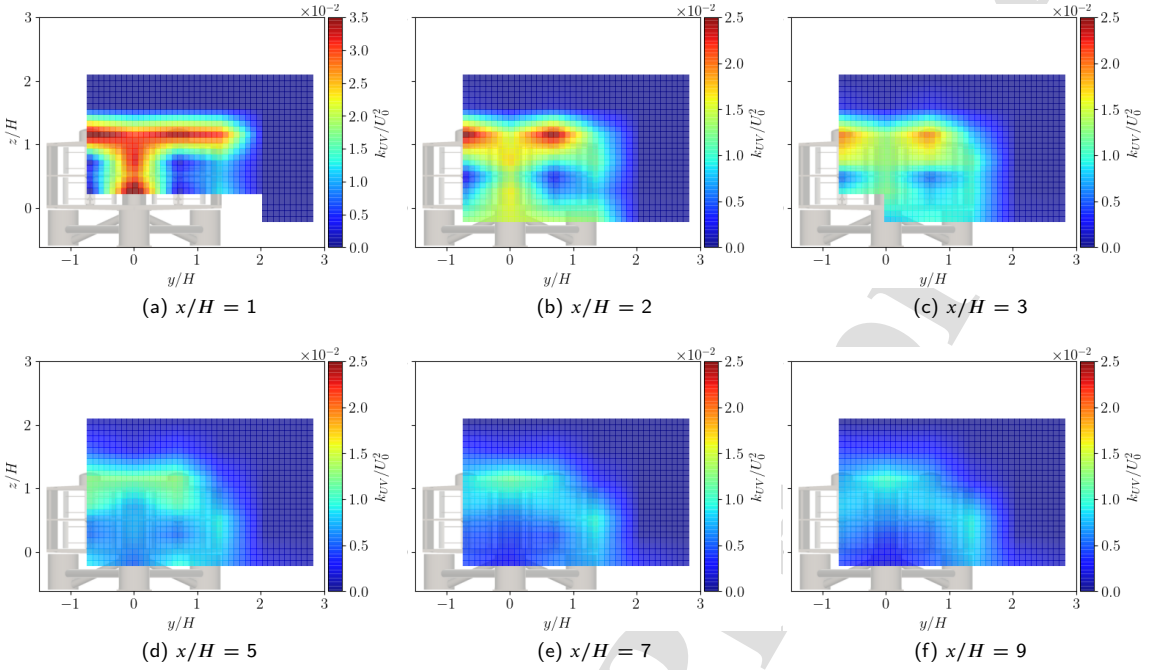

Figure 21: Ebb tide Configuration - Contours of the turbulent kinetic energy computed on u and v viewed from downstream. *nb*: the color scale is different in (a) compared to others.

shelters on top, in the counter-rotation direction similar to EC. They also observe large stationary swirls around the x axis behind each rotor column, centred on the top corners of the turbine. However, these swirls rotate in the opposite direction compared to our experimental results. This difference could be a combined effect of the base presence, the blockage in the tank and the difference of turbine scales or to some bias in the numerical model. The results in FC with the turbine fixed on the monopile (Appendix A, Fig. 28) show that the swirls rotate in the same direction whether on the monopile or on the tripod base, which tends to indicate that the base is not responsible for this difference between numerical and experimental results. However, this result is insufficient to exclude that the swirls would not rotate in the other direction in EC on the monopile. Our experiments show that those swirls are about 2 times stronger in FC than in EC, injecting more mean kinetic energy from the free-stream into the wake (Bachant and Wosnik, 2015; Rolin and Porté-Agel, 2018). Consequently, the overall wake recovers 30 % faster in FC than in EC and would reach $\overline{u}/U_0 = 0.9$ at $x/H = 16$ in FC while it would be at $x/H = 20$ in EC on the tripod base. Since our experiments are performed with a 1.5 % incident turbulence intensity, we can expect lower velocity deficits and faster recovery at full-scale where the turbulence intensity is mostly between 10 and 20 % (Filipot et al., 2015; Mycek et al., 2014; Grondeau et al., 2019).

Finally, from another perspective, this study also shows the influence of the gravity base geometry both on the performance and the wake of the ducted 2-VATT. Indeed, we showed that the presence of the base feet in front of the rotors in EC induces both flow asymmetry between the upper and the lower rotors and more turbulence that increase the torque fluctuations by 25 %. Besides, while the base geometry hardly affects the wake height of the turbine, it strongly impacts the width. The latter being the same right behind the turbine, the turbine far wake in FC is finally more than 30 % wider with the tripod than with the monopile. Furthermore, at the base altitude, the average velocity deficit is up to 30 % stronger behind the tripod than behind the monopile base. Thus, the velocity deficit behind the turbine is partly recovered by energy exchanges with the flow under it when the turbine is on the monopile while it is not possible on the tripod. As a consequence, the average velocity deficit in the turbine wake recovers 20 % faster on the monopile than on the tripod base. These results show the need to consider the base design with care to optimise both the performance and the wake in the perspective of tidal turbine arrays.

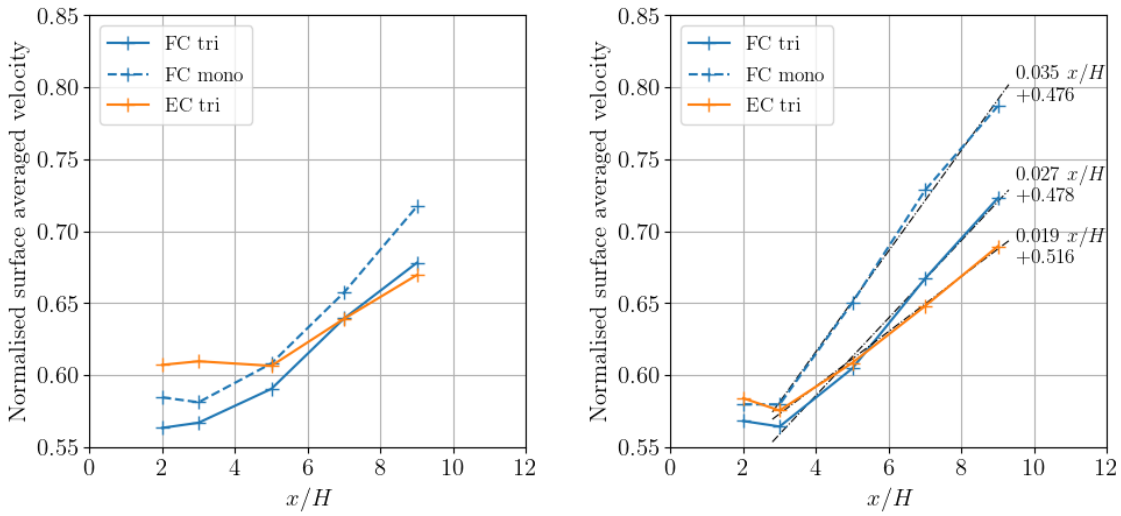

(a) $< \overline{u} >_{0.9}$ (b) $< \overline{u} >_{cap}$

Figure 22: Surface averages of the streamwise velocity at the 6 downstream positions in EC and FC (on tripod -solid line- and on monopile base -dashed line). (a) Average over the area where $\overline{u}/U_0 < 0.9$. (b) Average over the projected capture area of the turbine. The black lines are linear interpolations between the measurement points from $x/H = 3$ to 9.

In future works, the results presented in this paper will allow a better validation of the numerical models applied to twin vertical axis tidal turbines. Experiments in unsteady conditions such as turbulent flows or in presence of waves are also necessary to assess their effects on both the turbine performance and the wake development.

Acknowledgements

This work was financially supported in part by the Fench Research and Technology National Association (ANRT) under the convention Cifre n°2020/0688. The authors acknowledge Jean-Valéry Facq and Cédric Derveaux for the design of the turbine model as well as Benoît Gomez and Benoît Gaurier for their help during the experiments.

Data availability

The velocity measurement database presented in this study can be shared upon request to the authors.

References

Ahmadi, M.H., 2019. Influence of upstream turbulence on the wake characteristics of a tidal stream turbine. Renewable Energy 132, 989–997. doi:10.1016/j.renene.2018.08.055.

Bachant, P., Wosnik, M., 2015. Characterising the near-wake of a cross-flow turbine. Journal of Turbulence 16, 392–410. doi:10.1080/14685248.2014.1001852.

Bahaj, A., Molland, A., Chaplin, J., Batten, W., 2007. Power and thrust measurements of marine current turbines under various hydrodynamic flow conditions in a cavitation tunnel and a towing tank. Renewable Energy 32, 407–426. doi:10.1016/j.renene.2006.01.012.

Boutier, A. (Ed.), 2012. Laser Velocimetry in Fluid Mechanics. John Wiley & Sons.

Ebdon, T., Allmark, M.J., O'Doherty, D.M., Mason-Jones, A., O'Doherty, T., Germain, G., Gaurier, B., 2021. The impact of turbulence and turbine operating condition on the wakes of tidal turbines. Renewable Energy 165, 96–116. doi:10.1016/j.renene.2020.11.065.

Filipot, J.F., Prevosto, M., Maisondieu, C., Le Boulluec, M., Thomson, J., 2015. Wave and turbulence measurements at a tidal energy site, in: IEEE/OES 11th Current, Waves and Turbulence Measurement (CWTM), pp. 1–9. doi:10.1109/CWTM.2015.7098128.

Frost, C., Morris, C.E., Mason-Jones, A., O'Doherty, D.M., O'Doherty, T., 2015. The effect of tidal flow directionality on tidal turbine performance characteristics. Renewable Energy 78, 609–620. doi:10.1016/j.renene.2015.01.053.

Furgerot, L., Sentchev, A., Bailly du Bois, P., Lopez, G., Morillon, M., Poizot, E., Méar, Y., Bennis, A.C., 2020. One year of measurements in Alderney Race: preliminary results from database analysis. Philosophical transactions. Series A, Mathematical, physical, and engineering sciences 378, 20190625. doi:10.1098/rsta.2019.0625.

Gaurier, B., Ordonez-Sanchez, S., Facq, J.V., Germain, G., Johnstone, C., Martinez, R., Salvatore, F., Santic, I., Davey, T., Old, C., Sellar, B., 2020. MaRINET2 Tidal Energy Round Robin Tests—Performance Comparison of a Horizontal Axis Turbine Subjected to Combined Wave and Current Conditions. Journal of Marine Science and Engineering 8, 463. doi:10.3390/jmse8060463.

Grondeau, M., Guillou, S., Mercier, P., Poizot, E., 2019. Wake of a ducted vertical axis tidal turbine in turbulent flows, LBM actuator-line approach. Energies 12, 4273. doi:10.3390/en12224273.

Guillaud, N., 2017. Simulation et optimisation de forme d'hydroliennes à flux transverse. Ph.D. thesis. Grenoble Alpes.

Harrold, M., Ouro, P., 2019. Rotor Loading Characteristics of a Full-Scale Tidal Turbine. Energies 12, 1035. doi:10.3390/en12061035.

Hill, C., Neary, V.S., Gunawan, B., Guala, M., Sotiropoulos, F., 2014. U. S. Department of Energy Reference Model Program RM2 : Experimental Results. Technical Report. Sandia National Laboratories. Albuquerque. URL: https://www.osti.gov/servlets/purl/1171458.

Jégo, L., Guillou, S., 2021. Study of a Bi-Vertical Axis Turbines Farm Using the Actuator Cylinder Method. Energies 14, 5199. doi:10.3390/en14165199.

Jiang, Y., Zhao, P., Stoesser, T., Wang, K., Zou, L., 2020. Experimental and numerical investigation of twin vertical axis wind turbines with a deflector. Energy Conversion and Management 209, 112588. doi:10.1016/j.enconman.2020.112588.

Lam, H., Peng, H., 2017. Measurements of the wake characteristics of co- and counter-rotating twin H-rotor vertical axis wind turbines. Energy 131, 13–26. doi:10.1016/j.energy.2017.05.015.

Laws, N.D., Epps, B.P., 2016. Hydrokinetic energy conversion: Technology, research, and outlook. Renewable and Sustainable Energy Reviews 57, 1245–1259. doi:10.1016/j.rser.2015.12.189.

Masters, I., Malki, R., Williams, A.J., Croft, T.N., 2013. The influence of flow acceleration on tidal stream turbine wake dynamics: A numerical study using a coupled BEM–CFD model. Applied Mathematical Modelling 37, 7905–7918. doi:10.1016/j.apm.2013.06.004.

McNaughton, J., 2014. ReDAPT MC7.1: Initial operation power curve. Technical Report. Alstom Ocean Energy. URL: https://redapt.eng.ed.ac.uk/library/eti/reports/MC7.1InitialPowerCurve{_}A.pdf.

Moreau, M., Germain, G., Maurice, G., Richard, A., 2022. Sea states influence on the behaviour of a bottom mounted full-scale twin vertical axis tidal turbine. Ocean Engineering 265, 112582. doi:10.1016/j.oceaneng.2022.112582.

Moreau, M., Germain, G., Maurice, G., Richard, A., Coquet, R., 2021. HydroQuest : Feedback from Paimpol-Bréhat and validation of the design method, in: 14th European Wave and Tidal Energy Conference, Plymouth. pp. 2229–1–8.

Müller, S., Muhawenimana, V., Wilson, C.A., Ouro, P., 2021. Experimental investigation of the wake characteristics behind twin vertical axis turbines. Energy Conversion and Management 247, 114768. doi:10.1016/j.enconman.2021.114768.

Murray, R., 2016. Passively adaptive tidal turbine blades: Design methodology and experimental testing. Ph.D. thesis. Dalhousie University. URL: https://dalspace.library.dal.ca/handle/10222/72040.

Mycek, P., Gaurier, B., Germain, G., Pinon, G., Rivoalen, E., 2014. Experimental study of the turbulence intensity effects on marine current turbines behaviour. Part I: One single turbine. Renewable Energy 66, 729–746. doi:10.1016/j.renene.2013.12.036.

Rolin, V.F., Porté-Agel, F., 2018. Experimental investigation of vertical-axis wind-turbine wakes in boundary layer flow. Renewable Energy 118, 1–13. doi:10.1016/j.renene.2017.10.105.

Ross, H., Polagye, B., 2020. An experimental evaluation of blockage effects on the wake of a cross-flow current turbine. Journal of Ocean Engineering and Marine Energy 6, 263–275. doi:10.1007/s40722-020-00172-w.

Ross, H., Polagye, B., 2022. Effects of dimensionless parameters on the performance of a cross-flow current turbine. Journal of Fluids and Structures 114, 103726. doi:10.1016/j.jfluidstructs.2022.103726.

Vergaerde, A., De Troyer, T., Muggiasca, S., Bayati, I., Belloli, M., Kluczewska-Bordier, J., Parneix, N., Silvert, F., Runacres, M.C., 2020. Experimental characterisation of the wake behind paired vertical-axis wind turbines. Journal of Wind Engineering and Industrial Aerodynamics 206, 104353. doi:10.1016/j.jweia.2020.104353.

Zhou, Z., Benbouzid, M., Charpentier, J.F., Scuiller, F., Tang, T., 2017. Developments in large marine current turbine technologies – A review. Renewable and Sustainable Energy Reviews 71, 852–858. doi:10.1016/j.rser.2016.12.113.

A. Wake of the ducted 2-VATT in Flood Configuration on the monopile base

The appendix provides all the velocity contours and profiles presented in the Section 4 with the turbine on the monopile base instead of on the tripod in FC. Those data contribute to the discussion of the results and provide an extended database for numerical models validation.

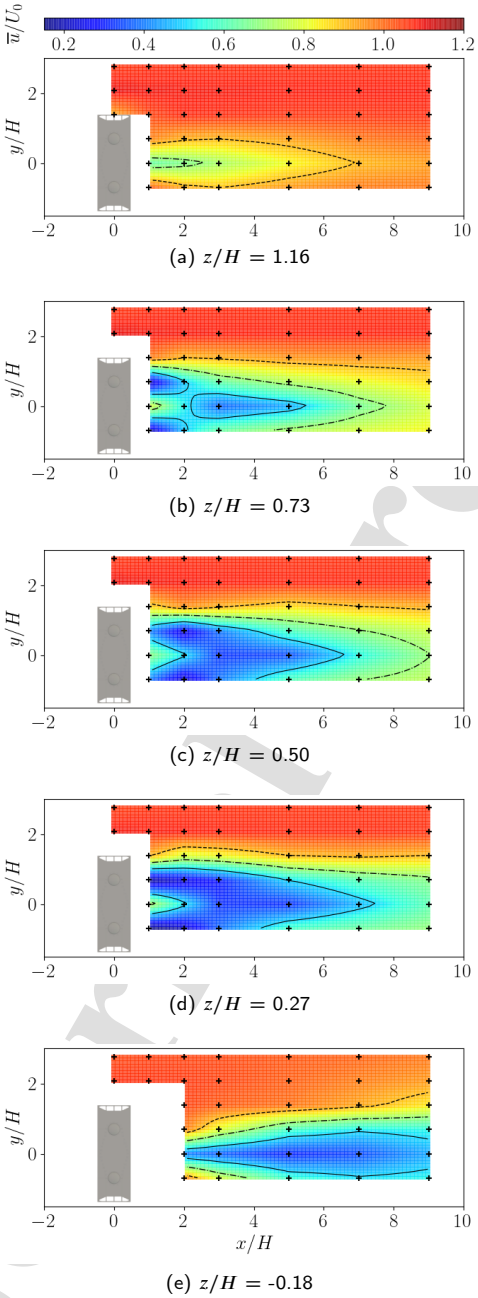

(a) $z/H = 1.16$

(b) $z/H = 0.73$

(c) $z/H = 0.50$

(d) $z/H = 0.27$

(e) z/H = -0.18

Figure 23: Contours of the streamwise velocity $(\overline{u}/U_0)$ at different altitudes in FC on the monopile base. The black crosses show the measurement point positions; the dashed, dash-dot and solid lines are iso-contours of $\overline{u}/U_0 = 0.9$, 0.7 and 0.5 respectively.

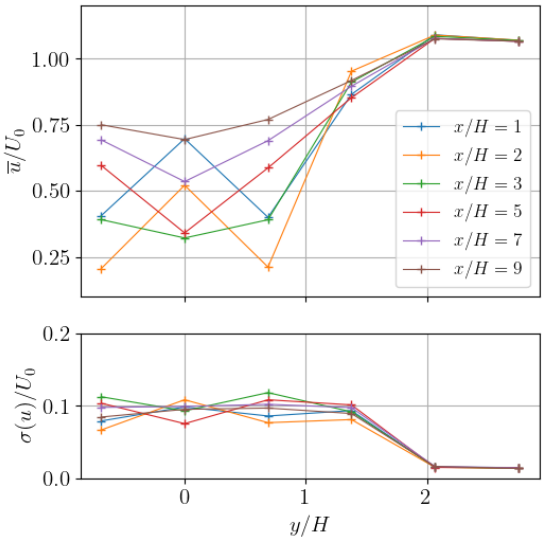

Figure 24: Horizontal streamwise velocity profiles at different downstream distances at the centre of the turbine ($z/H = 0.5$) in FC on the monopile base.

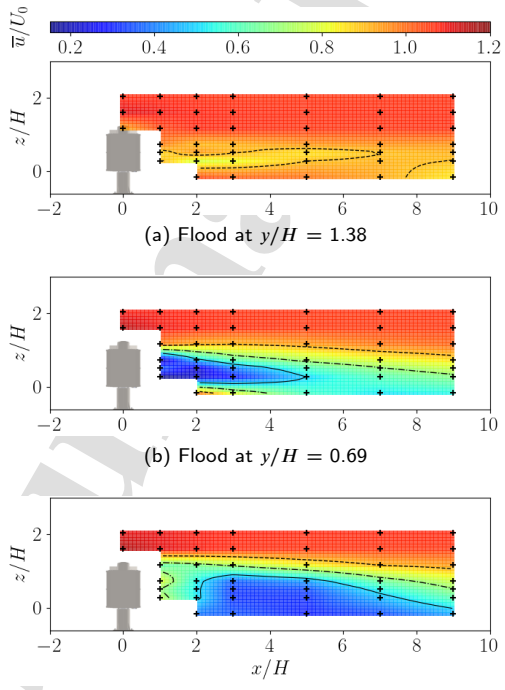

(a) Flood at $y/H = 1.38$

(b) Flood at $y/H = 0.69$

(c) Flood at $y/H = 0.00$

Figure 25: Contours of the streamwise velocity in the (y, z) plane at different positions along the width, in FC on the monopile base. The black crosses show the measurement point positions; the dashed, dash-dot and solid lines are iso-contours of $\overline{u}/U_0 = 0.9$, 0.7 and 0.5 respectively.

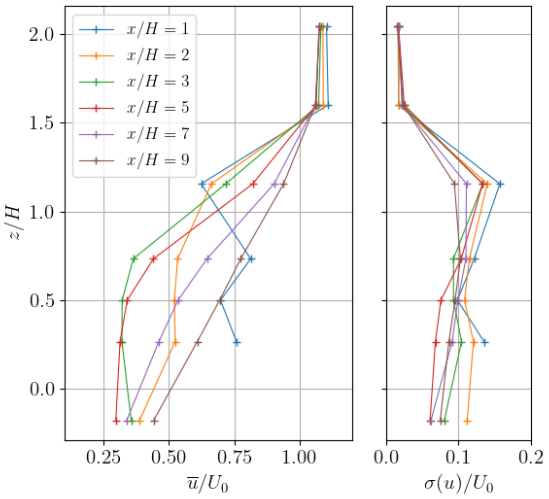

Figure 26: Vertical streamwise velocity profiles at different downstream distances at the center of the turbine ($y/H = 0.00$) in FC on the monopile base.

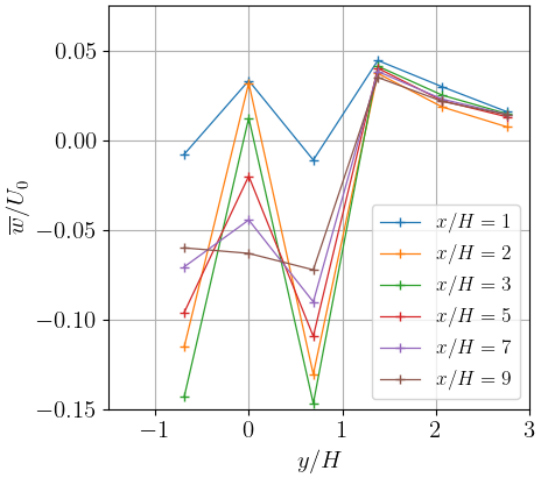

Figure 27: Horizontal profiles of mean vertical velocity at different downstream distances and $z/H = 0.73$, in FC on the monopile base.

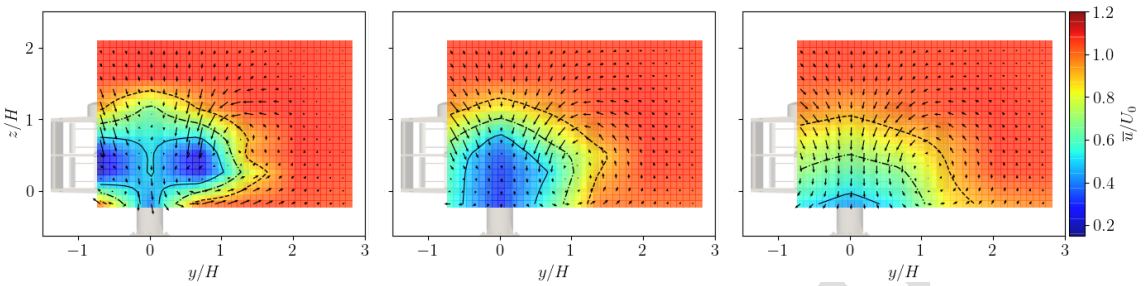

(a) $x/H = 2$ (b) $x/H = 5$ (c) $x/H = 9$

Figure 28: Contours of the mean streamwise velocity in (y, z) planes, viewed from downstream, with superimposition of arrow field of the mean transverse velocities $(\overline{v}, \overline{w})/U_0$ in FC on the monopile base; the dashed, dash-dot and solid lines are iso-contours of $\overline{u}/U_0 = 0.9$, 0.7 and 0.5 respectively.

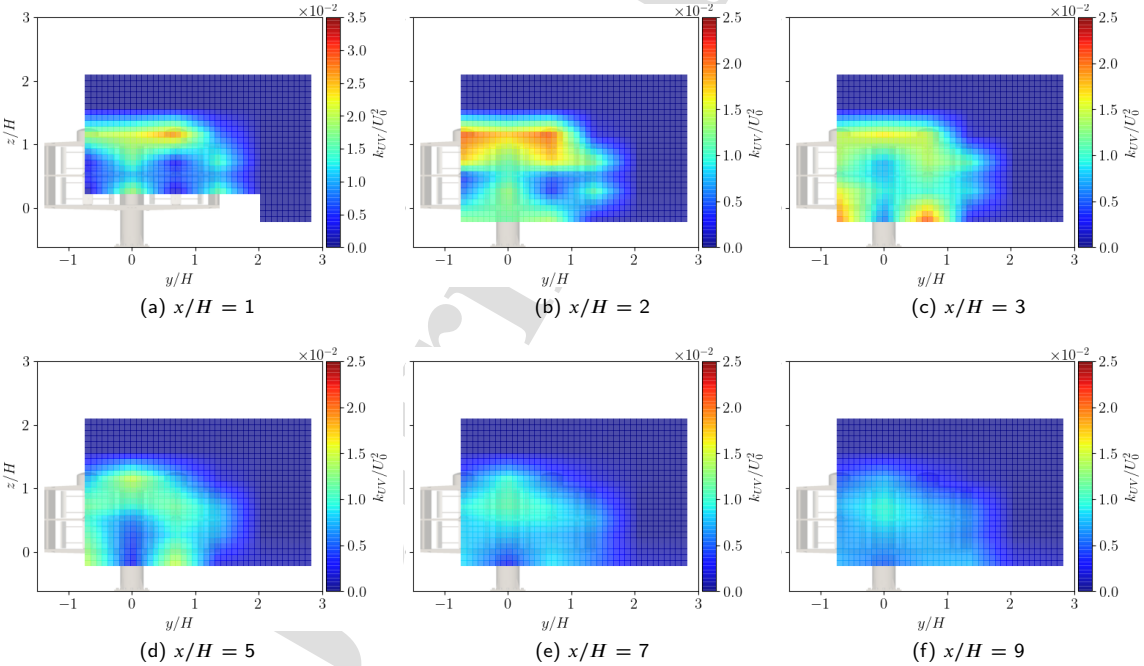

(a) $x/H = 1$ (b) $x/H = 2$ (c) $x/H = 3$

(d) $x/H = 5$ (e) $x/H = 7$ (f) $x/H = 9$

Figure 29: Contours of the turbulent kinetic energy computed on u and v viewed from downstream in FC on the monopile base. *nb*: the color scale is different in (a).

Author Contributions:

M. Moreau Methodology, Investigation, Software, Formal analysis, Writing - Original Draft, Visualization
G. Germain Conceptualization, Methodology, Investigation, Validation, Investigation, Writing - Review & Editing, Supervision, Funding acquisition
G. Maurice Conceptualization, Methodology, Validation, Supervision, Funding acquisition

Declaration of interests

X The authors declare that they have no known competing financial interests or personal relationships that could have appeared to influence the work reported in this paper.

☐The authors declare the following financial interests/personal relationships which may be considered as potential competing interests: